Boundary-Layer Meteorology (2020) 174:179–202
https://doi.org/10.1007/s10546-019-00481-0

RESEARCH ARTICLE

Contrasting Characteristics and Evolution of Southerly Low-Level Jets During Different Boundary-Layer Regimes

Timothy A. Bonin[1,2] · Petra M. Klein[1] · Phillip B. Chilson[1,3]

Received: 2 May 2018 / Accepted: 19 September 2019 / Published online: 17 October 2019

Abstract
Nocturnal low-level jets (LLJs) have been documented at many places around the world, particularly across the Great Plains of the United States. Nocturnal LLJs significantly affect the regional weather and climate, as well as several industrial activities. While the LLJ has been extensively studied, little attention has been paid to the relationship between the evolution of the LLJ, its properties, and the boundary-layer structure. Here, observations collected in northern Oklahoma, USA are used to analyze the characteristics and evolution of the LLJ during conditions of weak and strong turbulence, respectively, coinciding with strongly and weakly stable nocturnal boundary layers. Additionally, the relationship between the LLJ and the temperature profile under these different conditions is examined. Three case studies are used during conditions of weak and strong turbulence, followed by statistics computed from a larger dataset of LLJs. When turbulence is weak, the LLJ is shown to reach peak intensity later near sunrise, while a maximum in the intensity is reached about six hours after sunset in the highly turbulent boundary layer. Furthermore, the LLJ tends to stay constant with height when turbulence is maintained throughout the night, while the LLJ tends to follow isentropic surfaces when vertical mixing is suppressed. When the LLJ follows isentropic surfaces, changes in the wind speed are related to the stability modification.

Keywords Doppler lidar · Low-level jet · Stable boundary layer · Turbulence

1 Background

The low-level jet (LLJ) is a local wind-speed maximum typically observed at night in the lowest kilometre of the atmosphere when a stable boundary layer (SBL) develops. It is a prominent feature over the Great Plains of the United States (Bonner 1968). Several boundary-layer processes interact to produce the LLJ. The inertial oscillation contributes to the flow acceleration commencing around sunset; radiational cooling near the surface quells turbulent

✉ Timothy A. Bonin
timothy.bonin@ll.mit.edu

1 School of Meteorology, University of Oklahoma, Norman, OK 73072, USA

2 Present Address: MIT Lincoln Laboratory, Lexington, MA 02421, USA

3 Advanced Radar Research Center, University of Oklahoma, Norman, OK, USA

mixing of momentum rapidly, allowing the flow above the surface to accelerate to adjust to the mass field (Blackadar 1957; Van de Wiel et al. 2010; Klein et al. 2016). The gently sloping terrain over the Great Plains also contributes to its formation. Since the residual layer is tilted over the terrain, particularly during the summer months when baroclinicity is weak, horizontal gradients in buoyancy exist that cause the flow to accelerate over time when the boundary layer is stably stratified (Shapiro and Fedorovich 2009).

These LLJs directly affect several industrial and commercial sectors. The strong winds associated with LLJs amplify the energy production from wind farms (Storm et al. 2009), but the significant wind shear (up to 0.1 s^{-1}, Banta et al. 2003) can damage wind turbines (Sisterson and Frenzen 1978). Additionally, the strong shear associated with LLJs can mechanically generate turbulence (Banta et al. 2006), which decreases the energy production from wind plants (Vanderwende and Lundquist 2012). Aviation is also affected by LLJs, as wake vortices generated by aircraft are differentially advected with height due to the wind shear, affecting the period between consecutive aircraft landings (Kaplan et al. 2000). Low-level jets are also found to increase long-range transport and downward mixing for ozone and its precursor pollutants, which also affects near-surface ozone concentrations at night and during subsequent days (Klein et al. 2014). As such, understanding the interaction between the thermal stability, wind profile, and turbulence characteristics has ramifications for a variety of applications.

Generally, the nocturnal SBL is often categorized as a weakly stable boundary layer (wSBL) or very stable boundary layer (vSBL) depending on the associated turbulence, temperature, and wind profiles (Mahrt 2014). The type of nocturnal SBL that develops largely depends on the wind speed near the surface necessary to sustain turbulent mixing (Sun et al. 2012; Van de Wiel et al. 2012; Mahrt et al. 2015). For sufficiently large near-surface wind speeds, turbulence continues to be mechanically generated, which continuously warms the near-surface air that is radiatively cooling. However, little turbulence is generated mechanically when the wind speed is small, and a surface inversion forms that inhibits further vertical mixing.

Bonin et al. (2015) discuss general observed differences in temperature and turbulence profiles between both types of the SBL as observed at a site in northern Oklahoma. However, contrasting features of the evolution of the LLJ itself within a strongly turbulent wSBL or weakly turbulent vSBL have rarely been investigated previously, as past studies have produced statistics of the LLJ and its evolution (e.g., Bonner 1968; Mitchell et al. 1995; Whiteman et al. 1997; Song et al. 2005) without the ability to distinguish the turbulence characteristics of the SBL. Recent improvements in observational capabilities now allow a more comprehensive study of the LLJ and its evolution in relation to the SBL structure.

The LLJ has been linked closely with the temperature profile in the SBL. Baas et al. (2009) found that the LLJ is typically situated close to the top of the surface-based inversion, which is consistent with the Blackadar (1957) inertial oscillation theory. Bonner (1968) and Whiteman et al. (1997) both used radiosonde climatologies to study the Great Plains LLJ, and similarly found that the height of the LLJ is typically located above the top of the surface-based inversion with considerable variability. This variability can be largely explained by the complexity of the LLJ, as both the wind-speed and temperature profiles are affected by the magnitude of synoptic pressure gradients, irregularities in the terrain, soil moisture, cloud cover, precipitation, and other effects. In addition to these relationships with nocturnal inversions, Banta et al. (2002) found that the height of the LLJ sometimes followed the terrain, and at other times remained constant with height with respect to sea level. It is possible that the LLJ may follow one type of surface (terrain-following, height above sea-level, or isentropic) when associated with a strongly turbulent wSBL and another with a weakly turbulent vSBL.

Herein, observations from a Doppler lidar, an atmospheric emitted radiance interferometer (AERI), and radiosondes collected during the Lower Atmospheric Boundary Layer Experiment (LABLE) in the autumn of 2012 are used to investigate characteristics of the nocturnal LLJ. By combining these measurements, continuous time series of temperature, vertical velocity variance, and mean wind profiles are produced, providing a thorough depiction of the state of the boundary layer. These measurements are used to identify the SBL type and to observe the evolution of the LLJ to address the following questions:

1. Do the height and wind-speed maximum of the LLJ evolve differently for strongly turbulent and weakly turbulent SBLs? If so, why do they evolve differently?
2. How does the temperature profile and stability associated with the LLJ vary between the strongly turbulent and weakly turbulent SBL? Do consistent patterns and differences exist?

Information about the LABLE field campaign and the data processing techniques are provided in Sect. 2. To address the questions above, three case studies each of LLJs in the strongly and weakly turbulent SBL are presented within Sect. 3; for each case, the evolution of the LLJ and its characteristics are discussed. The relation of an LLJ to any surface-based or nocturnal inversion is discussed in Sect. 4. More general results of LLJ differences in weakly and strongly turbulent SBLs using all observations from the LABLE field campaign are presented in Sect. 5. The evolution of the height and strength of the LLJ is examined, including a discussion of a different process that may govern how the LLJ in the weakly turbulent vSBL evolves.

2 Experiment Overview

The LABLE field campaign (Klein et al. 2015) was conducted at the Atmospheric Radiation Measurement (ARM) Southern Great Plains (SGP) site, maintained by the United States Department of Energy (DOE). The ARM SGP site is surrounded by non-irrigated agricultural fields and the terrain is relatively flat (Wharton et al. 2015). Being located in north-central Oklahoma, USA, the site is near a geographic climatological maximum of the Great Plains LLJ (Bonner 1968; Song et al. 2005) and is ideally situated for studies of the LLJ and its characteristics. The Great Plains LLJ in particular significantly affects the weather and climate in the region (Stensrud 1996), and has been extensively studied for more than 50 years.

One of the primary objectives of the LABLE field campaign was to investigate the structure of the nocturnal SBL and its interaction with the LLJ, as addressed in Bonin et al. (2015). While the LABLE project was conducted in two phases, observations presented herein were collected during the LABLE-I phase, which occurred between 18 September and 13 November 2012. This study took place in autumn to observe the LLJ under a variety of synoptic situations, a time of year when the atmosphere is often baroclinic and LLJs are influenced by large-scale processes in addition to planetary boundary-layer (PBL) dynamics. This is in contrast to summertime in the Great Plains, when the troposphere is more often barotropic over the area.

During the LABLE-I field campaign, additional instruments including a Doppler lidar were deployed for the duration of the experiment to supplement the large array of instrumentation operating at the ARM SGP site. Details about the Doppler lidar and AERI observations, which are extensively used here, are provided below. In addition, measurements from radiosondes

that are routinely launched at the ARM SGP site at 0530, 1130, 1730, and 2330 UTC are used. A complete description of the radiosonde system can be found in Holdridge et al. (2011).

2.1 Doppler Lidars

During the LABLE-I field campaign, two Halo Streamline Doppler lidars were operated $\approx$ 300 m apart. One system is permanently installed at the SGP site and is maintained by the ARM program (Newsom 2012), while the other Doppler lidar was installed and operated by the University of Oklahoma (OU) for the campaign. Both systems have similar hardware and operated at 1.5 μm, and a data rate of $\approx$ 0.8 Hz, but they were operated differently. The OU system collected data at 18-m range gates, while the ARM lidar saved data at 30-m range gates. Thus, the ARM system had greater sensitivity under similar conditions, as additional subgates were averaged for each measurement. The minimum range of the OU lidar was 63 m and 75 m for the ARM system, and the maximum height coverage for both lidars was typically 1–2.5 km above ground level (all heights henceforth are as given above ground level), varying depending on aerosol content and other conditions.

The lidars each used a different scanning strategy. Every 15 min, the ARM Doppler lidar performed a plan-position indicator (PPI) scan using eight evenly spaced azimuths around the full compass at an elevation of 60°, which took about 1 min to complete. Otherwise, the ARM lidar was pointed vertically to measure fluctuations in the vertical-velocity component w. Every 30 min, the OU lidar performed consecutive PPI scans at both 40° and 70° elevations each at 72 azimuth positions taking $\approx$ 6 min to complete; otherwise, the OU system stared vertically to measure w. The mean wind profile from both systems was computed using measurements from each PPI scan with velocity azimuth display (VAD) analysis (Browning and Wexler 1968). Within our study, mean wind profiles from the OU lidar are used since the lower angle scan and shorter range gates enables higher-resolution wind profiles that begin closer to the surface. Additionally, the OU lidar wind measurements can be considered more precise, as precision generally increases with the number of beams in the VAD analysis (see Eq. 7 in Newsom et al. 2017). Wind observations from the OU lidar PPI 40° and 70° elevation scans are merged together to produce a single wind profile every 30 min. Vertical staring measurements from both Doppler lidars are used to calculate the vertical-velocity variance σ_w^2 over 30-min intervals. Random errors (i.e., instrument noise) are removed by using the autocovariance technique (Lenschow et al. 2000), exactly as described in Bonin et al. (2015).

2.2 Atmospheric Emitted Radiance Interferometer

The AERI instrument provides continuous thermodynamic soundings from observed atmospheric downwelling infrared radiation (Knuteson et al. 2004a, b). The AERI instrument measures a radiance spectrum spanning between the wavelengths of 3.3–19 microns (5.20–30.20 m^{-1}) at resolutions higher than 0.01 m^{-1}. Radiometric calibration better than 1% of the ambient radiance is maintained by measuring emissions from two well-characterized black bodies (one at 333 K, the other at ambient temperature) every 5 min.

A retrieval algorithm is used to transform observed spectra by the AERI instrument into thermodynamic soundings. First, the measured radiance spectra, which are each 30-s samples, are processed with a noise-filtering algorithm (Turner et al. 2006) and averaged over 5 min. Then, an optimal estimation retrieval algorithm (AERIoe, Turner and Löhnert 2014) is used to process the spectra for retrieval of profiles of temperature, as well as other properties

not used here. AERIoe is an iterative Newton–Gauss retrieval (Rodgers 2000) that uses a line-by-line radiative transfer model (Clough et al. 1992) to obtain retrieved thermodynamic variables from the observed radiance by the AERI instrument. To begin the retrieval, AERIoe needs an a priori dataset to serve as a first guess and background field. The hourly Rapid Refresh (RAP) model product is used to derive the a priori dataset, which is computed during post-processing using $\approx$ 2000 profiles from the RAP output over a 6-h moving window within a 260×260 km grid centred in time and space over nearest grid point to the AERI observation. For comparison with the Doppler lidar measurements that are provided every 30 m, the 5-min thermodynamic profiles are averaged over 30 min.

3 Case Studies

To investigate how LLJs evolve differently when the near-surface (defined as between 0–100 m) turbulence associated with the LLJs is strong or weak, several case studies are analyzed and compared. The turbulence regimes are categorized based on the measured $\overline{\sigma_w}_{,0-100}$ (the mean quantity of the standard deviation, σ_w, from the Doppler lidar below 100 m). Measurements from the OU Doppler lidar are used to calculate $\overline{\sigma_w}_{,0-100}$, as the shorter range gates are better able to resolve the small eddies that dominate near the surface. Since the lowest usable range gate is at 63 m, $\overline{\sigma_w}_{,0-100}$ values are truly a measure of σ_w between 63–100 m. During night-time conditions, Bonin et al. (2015) found that the vSBL formed when $\overline{\sigma_w}_{,0-100} < 0.2$ m s^{-1} and the wSBL existed when $\overline{\sigma_w}_{,0-100} > 0.2$ m s^{-1}. Similarly, the night-time (0200–1200 UTC) mean $\overline{\sigma_w}_{,0-100}$ is used here to categorize an LLJ as associated with a weakly turbulent vSBL if $\overline{\sigma_w}_{,0-100} < 0.2$ m s^{-1} and strongly turbulent wSBL if $\overline{\sigma_w}_{,0-100} > 0.2$ m s^{-1}.

Hereafter, the LLJ height Z_{LLJ} and wind-speed maximum V_{LLJ} are used to characterize the LLJ. The height Z_{LLJ} is taken to be the base of the LLJ (above which shear becomes small, less than 0.025 s^{-1}) and the wind speed V_{LLJ} is taken at Z_{LLJ} to characterize the LLJ height and strength. These criteria are used since LLJs may have a near-uniform wind profile above Z_{LLJ}, thus the height of a wind-speed maximum may be ambiguous. This definition is less stringent than the commonly used criterion from Bonner (1968) used in LLJ studies. A broader criterion is used here for two main reasons. First, our objectives rely on quantifying the evolution of the LLJ, thus main features of the LLJ (i.e., Z_{LLJ} and especially V_{LLJ}) must be tracked throughout the entire night, even before an LLJ forms that meets the more rigid definition. Second, the Bonner (1968) definition requires a wind-speed minimum to be detected above the LLJ at a height up to 3 km. Often, the Doppler lidar does not measure the wind profile beyond 1.5 km due to a low signal-to-noise ratio, so it is not always possible to detect a wind-speed minimum above an LLJ with Doppler lidar data. This broader criterion must be considered when interpreting results herein going forward, particularly when analyzing Z_{LLJ} early in the night before an LLJ maximum truly forms.

Case studies are presented for three nights when LLJs formed associated with a vSBL, and three for LLJs that formed in a wSBL. For the cases presented, no clouds beneath 3-km were detected over the ARM SGP site by a ceilometer at any point during the night. However, based on infrared satellite observations, high cirrus were observed at some point during every night except for 8 November. For each case, the evolution of wind speed, wind direction, vertical velocity variance, and thermodynamic profiles are shown and discussed. While the synoptic conditions certainly affected the LLJ evolution, the set-up was often complex and varied considerably for each case. Investigating the synoptic influence on the LLJ is largely beyond the scope of this study as the focus is on the PBL dynamics associated with the LLJ. The

Table 1 Summary of mean statistics of the southerly LLJs observed during the LABLE field campaign used in this study; several LLJs are omitted when an instrument was not operating or there was a frontal passage overnight. Date given (in UTC) when the LLJ was observed. Direction is the mean direction at Z_{LLJ} over the night. Max V_{LLJ} is maximum wind speed overnight with the LLJ. $\overline{Z_{LLJ}}$ is the mean height of the LLJ, while σZ_{LLJ} is the standard deviation around that mean. $\overline{\sigma_w}_{,0-100}$ is the standard deviation of the vertical velocity in the lowest 100-m, as observed by the Doppler lidar, which is used to classify the boundary-layer type. All of the values are computed over 0200–1200 UTC. The LLJs examined as case studies in Sect. 3 are highlighted in grey

Date [day/month]	Direction [° from]	Max V_{LLJ} [m s^{-1}]	$\overline{Z_{LLJ}}$ [m]	σZ_{LLJ} [m]	$\overline{\sigma_w}_{,0-100}$ [m^2 s^{-2}]	Classification
09/10	197	23.7	365	99	0.10	vSBL
12/10	215	17.7	647	290	0.10	vSBL
13/10	191	28.6	557	109	0.27	wSBL
16/10	214	27.4	349	42	0.47	wSBL
20/10	232	19.4	727	295	0.06	vSBL
21/10	194	19.0	417	103	0.07	vSBL
22/10	198	31.1	600	83	0.52	wSBL
23/10	206	27.8	614	186	0.47	wSBL
24/10	205	26.7	475	47	0.54	wSBL
29/10	161	12.0	99	28	0.09	vSBL
01/11	174	12.0	218	226	0.09	vSBL
02/11	186	20.6	507	274	0.08	vSBL
08/11	163	27.4	300	107	0.07	vSBL
09/11	206	31.7	681	119	0.50	wSBL
10/11	206	34.4	693	130	0.63	wSBL

synoptic influence is only discussed where it is necessary to explain observed phenomena. The presented cases are chosen to represent the variability of the LLJ within each SBL type, as observed during the LABLE-I field campaign. A summary of key statistics of the observed southerly LLJs during the LABLE-I field campaign is provided in Table 1.

3.1 Southerly Low-Level Jets Associated with a Very Stable Boundary Layer

Over the course of the LABLE-I field campaign, eight southerly LLJs associated with a vSBL with maximum wind speeds, V_{LLJ}, greater than 12 m s^{-1} were observed. While these are classified as weakly turbulent vSBLs based on the value of σ_w ($\overline{\sigma_w}_{,0-100}$) from the Doppler lidar, several of these LLJs were associated with intermittent periods of elevated mixing disconnected from the surface. Three of these cases are discussed in detail below.

3.1.1 9 October 2012

The LLJ that formed on 9 October slowly strengthened overnight between 0000–1000 UTC, when wind speed reached a maximum, as shown in Fig. 1a. Coincident with the slow strengthening of the LLJ, the stability within the layer where the LLJ formed also increased overnight. This increase in stability is due to radiative cooling at the surface and warming in the layer from 600–1000 m due to warm-air advection apparent on upper-air charts (not shown). Over this time period, the LLJ core, defined as the depth where the wind speed is greater than $0.75V_{LLJ}$ and shown by the white dashed lines in Fig. 1, became more narrow over time. Additionally, Z_{LLJ} tended to follow an isentropic surface throughout the night. As the surface-based inversion deepened overnight, Z_{LLJ} also increased.

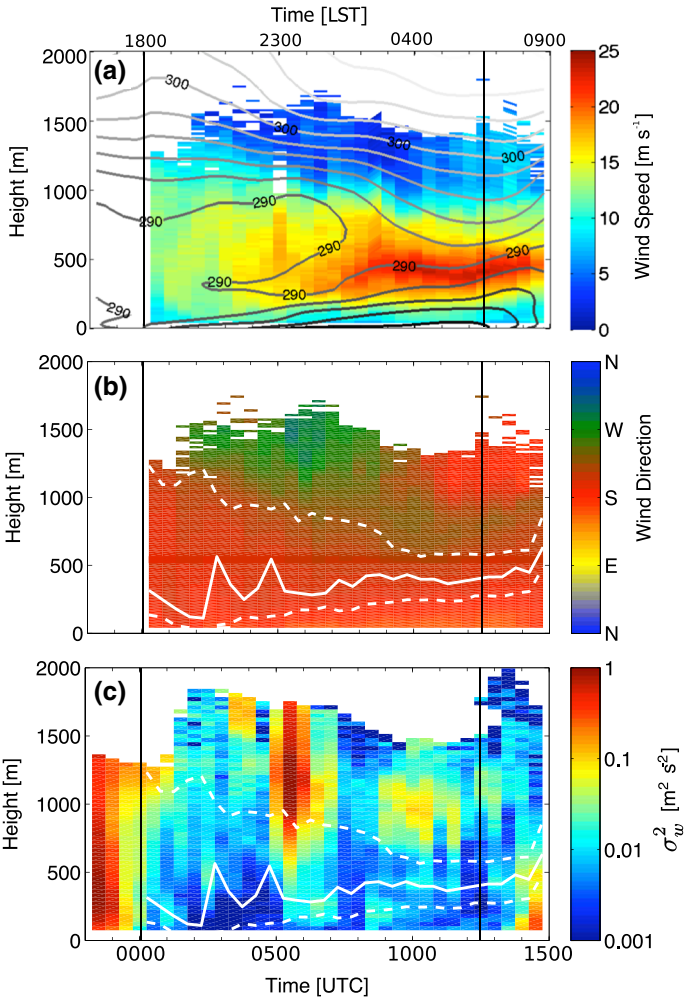

Fig. 1 Time–height cross-sections of wind speed overlaid with isentropes contoured every 2 K where darker colours indicate lower potential temperature (**a**), wind direction (**b**), and vertical velocity variance (**c**) on 9 October 2012. The solid white lines indicate the height of the LLJ, while the dashed lines show where the wind speed is 75% of the wind-speed maximum, indicating the relative width of the LLJ. Sunset and sunrise are marked by the two vertical black lines

Throughout the night, the wind direction within the LLJ core remained relatively constant (Fig. 1b). Above the LLJ, the wind direction generally turned westerly with height, until about 1000 UTC when an approaching trough shifted the winds to become southerly above 1 km. The directional change in wind direction with height within the core of the LLJ remained relatively constant throughout the night; that is, as the LLJ core became more narrow overnight, the directional shear $d\varphi/dz$ increased as the depth of the core decreased.

Just before sunset, mixing throughout the PBL rapidly decayed as shown by the large decrease in σ_w^2 in the two hours before 0000 UTC in Fig. 1. After this, through much of the night, values of σ_w^2 below the jet remained quite small and less than 0.01 m^2 s^{-2}. An increase in σ_w^2 below the LLJ is observed shortly after 0500 UTC. In addition, pronounced waves with

periodic rising and sinking motion became apparent above the LLJ starting at 0500 UTC and continued intermittently throughout the rest of the night. The waves were identified on time-height cross-sections of w and signal-to noise ratio from the Doppler lidar. The waves were not pure, as turbulence was generated through a process discussed by Finnigan et al. (1984).

3.1.2 21 October, 2012

Similar to the LLJ that developed on 9 October, the LLJ on 21 October did not develop until $\approx$ 6 hr after sunset, as shown in Fig. 2. While the wind speed quickly increased after sunset through a layer extending from just above the surface to 1 km, which is to be expected with the rapid reduction in frictional effects, the wind speed within that layer remained relatively constant with height for several hours. Simultaneously, a surface-based inversion began to form around sunset when the PBL mixing decreased and wind speeds increased. While turbulence rapidly decayed near the surface it persisted for several hours after sunset in the residual layer between 250–1200 m.

In the hours after sunset, the surface-based inversion continued to intensify and deepen over time. However, the layer from 250–1200 m remained nearly dry adiabatic until 0500 UTC, which coincided with the aforementioned period when turbulent mixing within this layer persisted. During this time period, the wind direction remained relatively constant with height, although a veering profile began to develop after 0500 UTC when the elevated mixing diminished.

Between 0600–0700 UTC, a well-defined LLJ rapidly formed as the maximum wind speed increased from 12 m s^{-1} to 20 m s^{-1}. This coincided with a large increase in stability in the layer from 500–1200 m over a short period of time. While the reason for the rapid increase in elevated stability is not entirely clear, it is likely due to significant warm-air advection increasing with height and/or large-scale subsidence coincident with a 500-hPa ridge over the area. As the LLJ strengthened between 0600–0700 UTC, directional wind shear also increased as $d\varphi/dz$ became larger, especially within the LLJ core. The wind direction became more westerly with height. During this time period, values of σ_w^2 remained small throughout the lowest 1 km, although some periods of weak intermittent mixing occurred.

3.1.3 8 November 2012

Similarly to the LLJ on 9 and 21 October, the LLJ on 8 November developed several hours after sunset after a surface-based inversion already formed, as shown in Fig. 3. After the daytime turbulent mixing within the PBL diminished around sunset, the wind speed within the lowest 1 km slowly increased throughout the night. The maximum wind speed of $\approx$28 m s^{-1} occurred at 1400 UTC, shortly before daytime mixing redistributed the momentum through a deeper layer. As the surface-based inversion grew throughout the night, Z_{LLJ} generally increased as well, coinciding well with the top of the nocturnal inversion. Additionally, stability within the LLJ slowly increased until about 1400 UTC coinciding with its strengthening. However, the stability near the ground decreased slightly after 1000 UTC due to weak mechanical mixing indicated in Fig. 3c.

Around sunset, a directional-wind-shear layer was apparent at 1200 m; this wind shear was located at the top of the PBL, wherein the layer below was well-mixed. As the PBL collapsed and daytime mixing ceased, the large $d\varphi/dz$ at this height slowly decreased over the following hours. During this decrease in $d\varphi/dz$, elevated mixing is still evident within the layer of strong directional shear while turbulence near the surface decayed. The directional

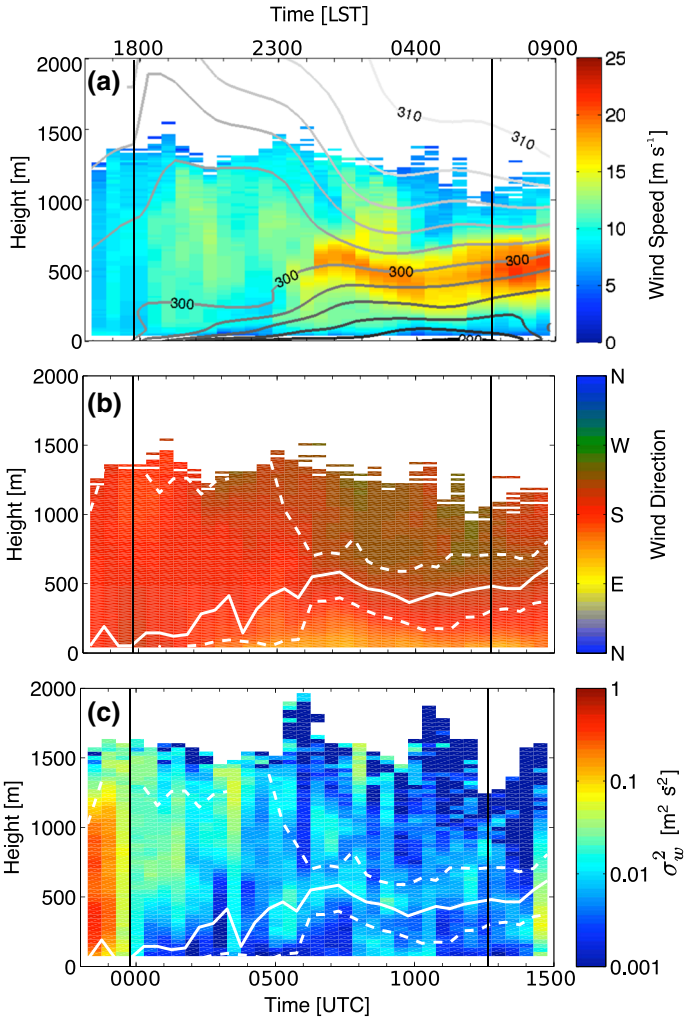

Fig. 2 Time–height cross-sections of wind speed overlaid with isentropes contoured every 2 K where darker colours indicate lower potential temperature (**a**), wind direction (**b**), and vertical velocity variance (**c**) on 21 October 2012. The solid white lines indicate the height of the LLJ, while the dashed lines show where the wind speed is 75% of the wind-speed maximum, indicating the relative width of the LLJ. Sunset and sunrise are marked by the two vertical black lines

shear sustained turbulence within this layer for several hours until the shear itself decayed. Throughout the rest of the night, the wind direction within the lowest 1 km generally became more westerly with both height and time.

Similarly to the previous two LLJs associated with weak turbulence in the vSBL, values of σ_w^2 remained small within and below the LLJ core for most of the night. However, intermittent turbulent mixing occured throughout the night, such as at 0800 UTC at 250 m. The higher values of σ_w^2 above 1 km at around 1000 UTC are due to waves propagating across the SGP site, visible on time–height cross-sections of w (not shown).

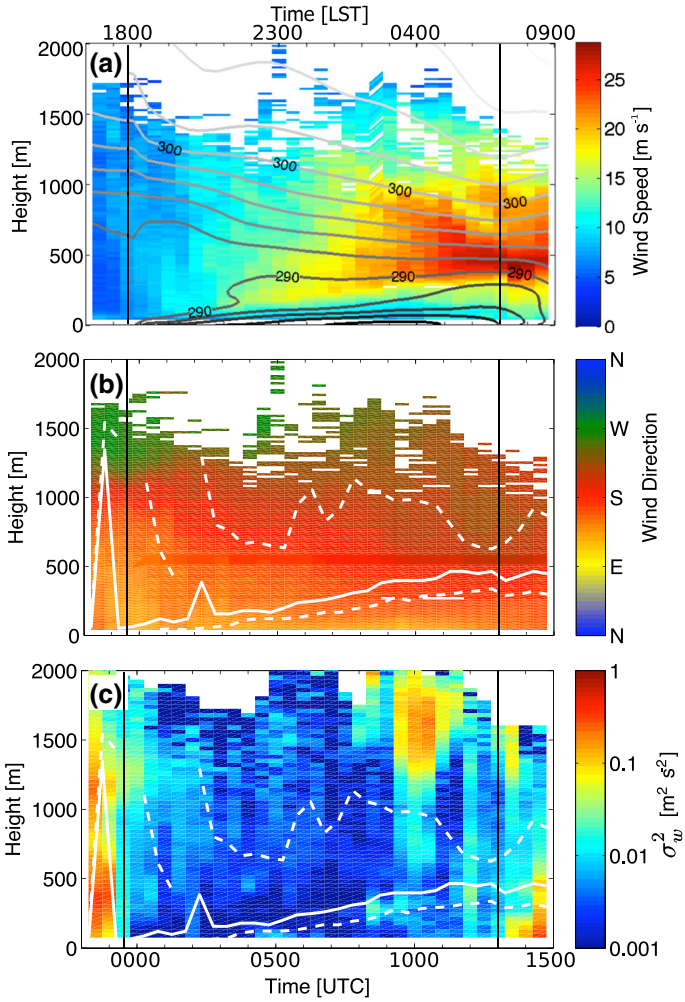

Fig. 3 Time–height cross-sections of wind speed overlaid with isentropes contoured every 2 K where darker colours indicate lower potential temperature (**a**), wind direction (**b**), and vertical velocity variance (**c**) on 8 November 2012. The solid white lines indicate the height of the LLJ, while the dashed lines show where the wind speed is 75% of the wind-speed maximum, indicating the relative width of the LLJ. Sunset and sunrise are marked by the two vertical black lines

3.2 Southerly Low-Level Jets Associated with a Weakly Stable Boundary Layer

Seven nights when LLJs were associated with a turbulent wSBL are used in this study; many of these LLJs occurred on consecutive periods. For example, the nights of 22–24 October and 9–11 November (11 November excluded from study, as a cold front passed at 0800 UTC) had LLJs that generated strong turbulence below their core. Most of the time, strong near-surface turbulence was persistent throughout the whole night. The near-surface wind speed around sunset was sufficiently large ($>$ 10 m s^{-1}) to maintain turbulence throughout the evening transition period. However, on a few occasions the near-surface σ_w^2 decreased after sunset before mixing re-established later, such as on 9 November discussed in Sect. 3.2.3.

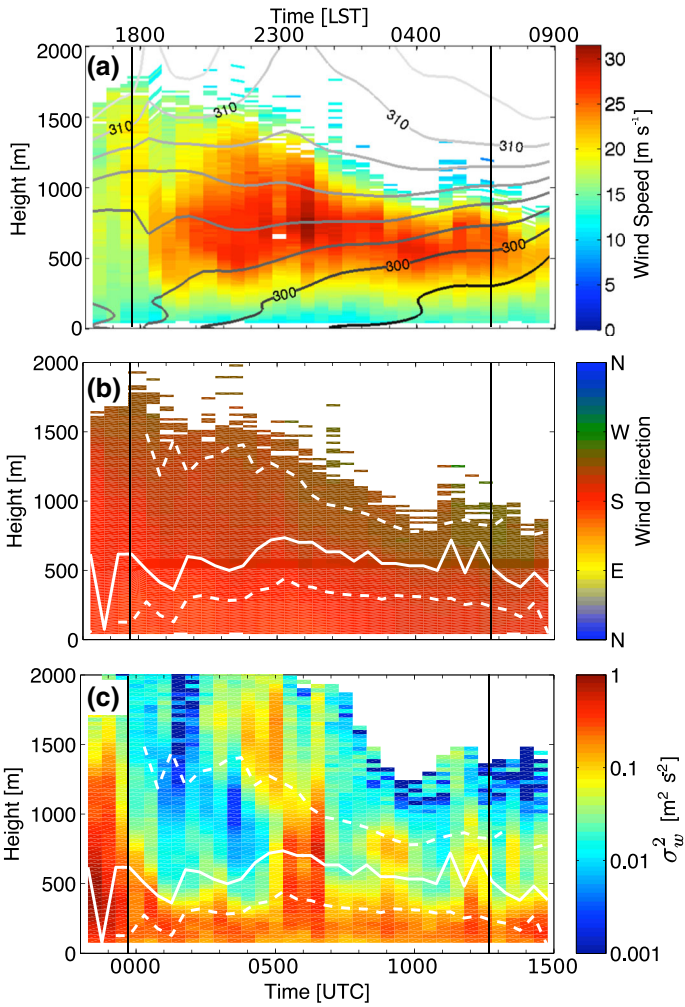

Fig. 4 Time–height cross-sections of wind speed overlaid with isentropes contoured every 2 K where darker colours indicate lower potential temperature (**a**), wind direction (**b**), and vertical velocity variance (**c**) on 22 October 2012. The solid white lines indicate the height of the LLJ, while the dashed lines show where the wind speed is 75% of the wind-speed maximum, indicating the relative width of the LLJ. Sunset and sunrise are marked by the two vertical black lines

3.2.1 22 October 2012

The LLJ on 22 October rapidly developed after sunset, as shown in Fig. 4. The LLJ remained relatively broad as the LLJ core, where the wind speed $> 0.75V_{LLJ}$, was deeper than 1 km for several hours after sunset. The LLJ became narrower over time, and concurrently the LLJ strengthened until about 0600 UTC when Z_{LLJ} reached a maximum. After 0600 UTC, V_{LLJ} gradually decreased. The wind direction remained generally southerly near the surface. Directional shear continuously increased overnight, as $d\varphi/dz$ reached a maximum in the early morning hours before sunrise.

No surface-based inversion formed with the LLJ, although the entire layer below 600 m slowly cooled. Concurrently, values of σ_w^2 beneath the LLJ remained relatively large ($>$ 0.1 m^2 s^{-2}) throughout the entire night. The absence of a surface-based inversion enabled the mixing to continue, further preventing the development of a low-level inversion through downward transport of warmer air to replace the air that is radiatively cooled in a positive feedback cycle. Several times, such as at 0500 UTC and 0900 UTC, waves were apparent within and above the LLJ core. Interactions between these waves and the PBL enhanced turbulent mixing in the lower levels during these times. The observed waves may be an undular bore produced by the cold front in Kansas impinging on the nocturnal stable layer (e.g. Clarke et al. 1981; Koch et al. 1991).

3.2.2 24 October 2012

The LLJ on 24 October developed particularly early, as a pronounced wind-speed maximum was evident at 2200 UTC at 600 m in Fig. 5. This LLJ developed 2 hr before sunset, during the afternoon-to-evening transition (Mahrt 1981; Grimsdell and Angevine 2002). The LLJ strengthened until 0300 UTC, when V_{LLJ} reached a maximum and remained nearly constant until 1000 UTC, when the LLJ abruptly weakened. This weakening was corroborated by sonic anemometery at the SGP site, as the wind speed at 60 m decreased from 14 m s^{-1} to 11 m s^{-1} over 30 min. The height of the LLJ was approximately constant overnight at 500 m, while the depth of the core decreased slowly overnight as the LLJ became more intense. Similarly to previously discussed LLJs, the wind direction became more westerly with height overnight, and $d\varphi/dz$ was largest at $\approx$1200 UTC.

Since substantial turbulent mixing below the LLJ continued throughout the night, no significant surface-based inversion formed again. Still, stability increased below Z_{LLJ} as air cooled near the surface was distributed throughout the entire layer by the turbulent mixing. Above Z_{LLJ}, where values of σ_w^2 were smaller, the layer of air generally warmed likely due to warm-air advection. The increase in σ_w^2 through a deeper layer up to 1 km at 1100 UTC is due to waves that moved over the ARM SGP site, which are apparent in the Doppler lidar observations of w (not shown). These waves exhibit a similar signature of distinct periodic rising and sinking motions as those on other nights.

3.2.3 9 November 2012

The evolution of the LLJ on 9 November was different than the previous two LLJs that maintained turbulent mixing through the evening transition period. The LLJ developed more slowly, as shown in Fig. 6, as V_{LLJ} did not increase rapidly after sunset. Starting at 0100 UTC and until 0600 UTC, V_{LLJ} increased from 16 m s^{-1} to 32 m s^{-1}; additionally, the LLJ subsided during the time period from $\approx$1 km to 600 m. After 0800 UTC, V_{LLJ} started to decrease, which continued throughout the rest of the night. Over the entire night, the wind direction near the surface remained south-south-westerly. However, above 500 m, the wind direction became more westerly overnight, likely in response to the passage of a 850-hPa shortwave trough. Similarly to previous nights, values of $d\varphi/dz$ increased over the course of the night.

While no strong surface-based inversion formed on 9 November, a weak inversion began to form shortly after sunset. During this time period, the near-surface wind was weak, and turbulent mixing that was present during the day was rapidly decaying throughout the entire depth of the PBL. While the near-surface turbulent mixing never became as weak as during the

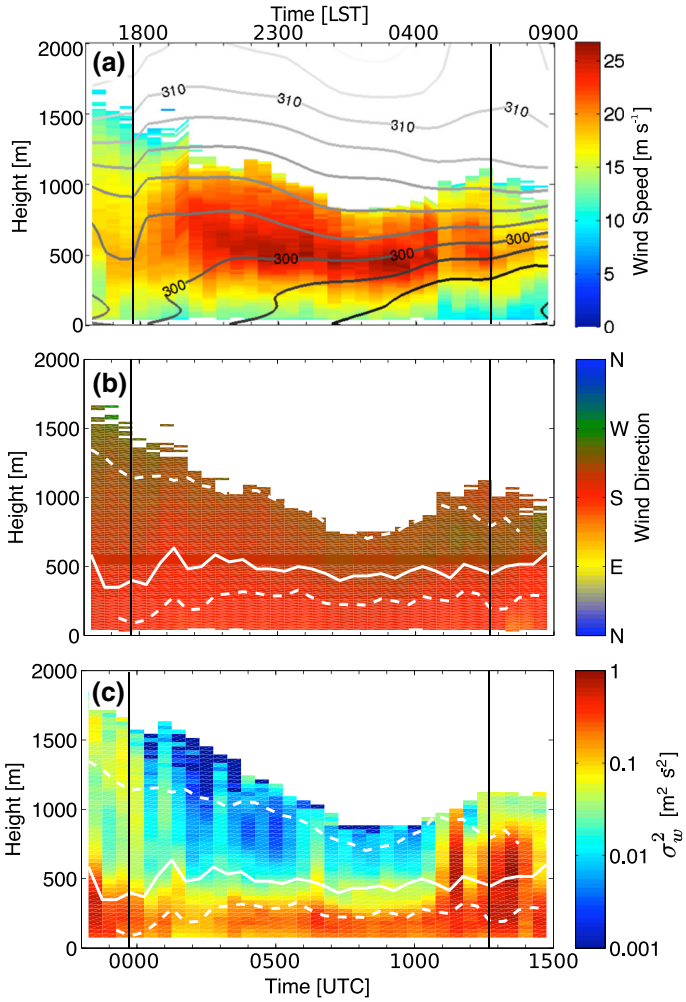

Fig. 5 Time–height cross-sections of wind speed overlaid with isentropes contoured every 2 K where darker colours indicate lower potential temperature (**a**), wind direction (**b**), and vertical velocity variance (**c**) on 24 October 2012. The solid white lines indicate the height of the LLJ, while the dashed lines show where the wind speed is 75% of the wind-speed maximum, indicating the relative width of the LLJ. Sunset and sunrise are marked by the two vertical black lines

vSBL cases, it was substantially less than on both 22 and 24 October from 0000–0400 UTC. At 0400 UTC, as the LLJ was descending, more substantial turbulent mixing ($\sigma_w^2 > 0.1\,\mathrm{m^2\,s^{-2}}$) occurred underneath the jet. Between 0400–0500 UTC, this turbulent mixing became connected with the surface as it eroded the weak surface-based inversion that formed, which is shown in Fig. 6. Afterwards, the turbulent mixing remained connected to the surface for the remainder of the night. As with many other LLJs, waves passed over the ARM SGP site multiple times over the night, which show up as large increases in σ_w^2 often on the order of $1\,\mathrm{m^{-2}\,s^{-2}}$.

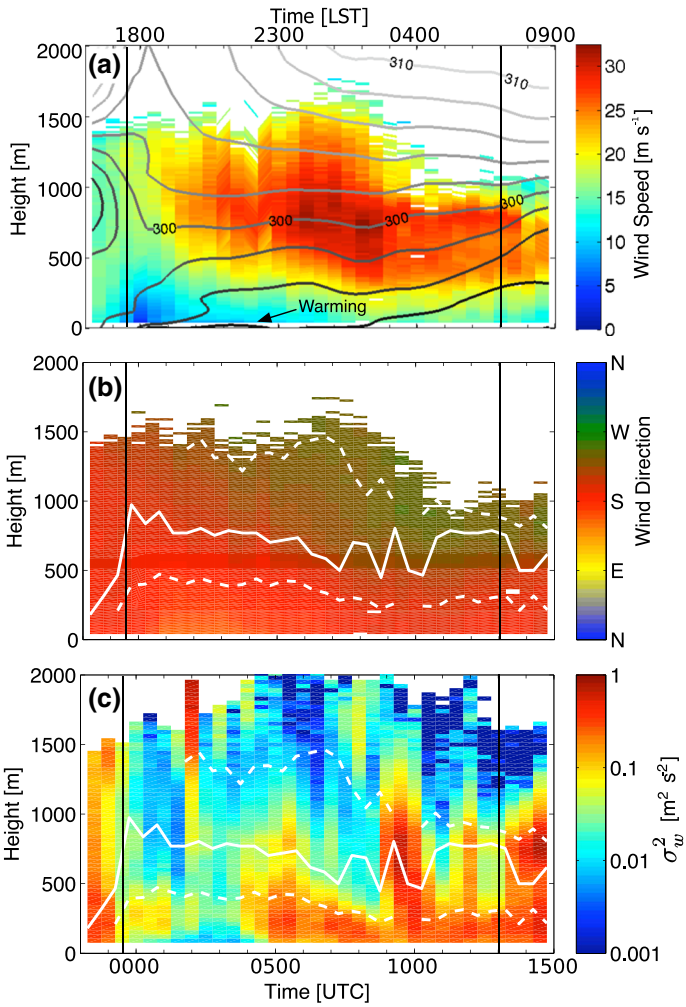

Fig. 6 Time–height cross-sections of wind speed overlaid with isentropes contoured every 2 K where darker colours indicate lower potential temperature (**a**), wind direction (**b**), and vertical velocity variance (**c**) on 9 November 2012. The solid white lines indicate the height of the LLJ, while the dashed lines show where the wind speed is 75% of the wind-speed maximum, indicating the relative width of the LLJ. Sunset and sunrise are marked by the two vertical black lines

4 Inversion Location

4.1 Low-Level Jets Associated with a Very Stable Boundary Layer

In Fig. 7, the mean wind speed is overlaid with the temperature profile for the LLJ cases discussed in Sect. 3.1. All the temperature data shown in these plots are from radiosondes, which are capable of resolving elevated inversions and small temperature changes that often cannot be resolved by the AERI instrument. On 9 October at 0600 UTC, the nose of the LLJ was broad, with the wind speed being ≈16–17 m s^{-1} over a layer extending from 250–700 m, as shown in Fig. 7a. This region was bounded by two inversions on the top and on the bottom.

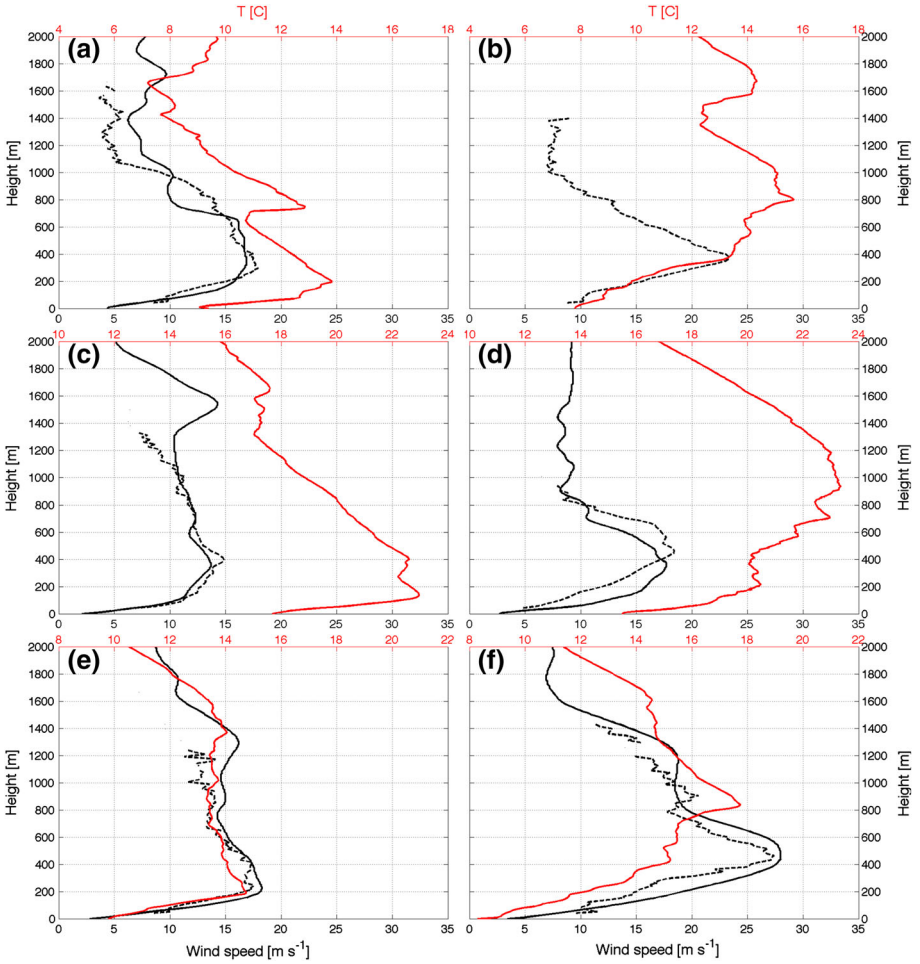

Fig. 7 Profiles of temperature and wind speed during time periods when LLJs were associated with weak near-surface turbulence and a vSBL. Red lines show the temperature measured by the radiosonde, and black shows the wind speed from the OU Doppler lidar (dashed) and radiosonde (solid). Profiles are for the cases discussed in Sect. 3.1: 9 October (**a**, **b**), 21 October (**c**, **d**), and 8 November (**e**, **f**). Left column is from profiles at approximately 0600 UTC, right is at 1200 UTC. Radiosonde and Doppler lidar observations may be up to 15 min apart

Between 0600–1200 UTC, the layer above 400 m but below the upper inversion warmed. During this time, V_{LLJ} increased and the shear associated with the LLJ also increased, as a pronounced well-defined LLJ nose formed. This coincided with the increase in stability discussed within Sect. 3.1.1. By 1200 UTC on 9 October, the LLJ nose was located at the top of the surface-based inversion, defined by the inflection point in the lapse rate. Above this layer, warm-air advection is apparent based on the increasing temperature between 0600 and 1200 UTC (Fig. 7a,b). This is corroborated by the 850-hPa analysis (not shown), as a south-west wind advected warm air across a temperature gradient increasing from east to west.

Profiles at both 0600 UTC and 1200 UTC over 21 October are shown in Fig. 7c,d. At 0600 UTC, two wind-speed maxima were present at 400 m and 1500 m, although the Doppler lidar was only able to measure the lower maximum due to a reduced signal-to noise ratio above

1300 m. Between the two maxima, there was a relatively broad area with wind speeds greater than 10 m s^{-1}. The maximum at 400 m was located at the top of an inversion. The second maximum was located within an isothermal layer between two nearly dry-adiabatic regions. Additionally, the wind-speed profile has a kink at the top of the surface-based inversion. By 1200 UTC, the layer above 550 m warmed resulting in a deep elevated inversion between 400–900 m, as shown in Fig. 7 d. Between 0600–1200 UTC, as this layer warmed, V_{LLJ} increased and the shear associated with the jet also increased. The LLJ at 1200 UTC was located underneath an elevated inversion and just above the surface inversion.

At 0600 UTC on 8 November, an LLJ nose was collocated with the top of a strong surface-based inversion at 200 m (see Fig. 7e), as observed in previous studies (Baas et al. 2009). Again, a secondary wind-speed maxima is evident at 1300 m. By 1200 UTC, Z_{LLJ} was about twice as high as it was at 0600 UTC, coinciding with the surface-based inversion growing deeper overnight. Additionally, the top of the LLJ was collocated with an elevated inversion at ≈800 m. Throughout all six profiles, the height of the LLJ was located at or just above the top of the surface-based inversion, defined by the inflection point in the temperature profile.

4.2 Low-Level Jets Associated with a Weakly Stable Boundary Layer

Similar comparisons between the temperature and wind-speed profiles are made for LLJs associated with a turbulent wSBL within Fig. 8. None of the LLJs shown here was associated with surface-based inversions due to the continued vertical mixing overnight. On 22 October, Z_{LLJ} coincided with the location of an elevated inversion at 650 m, as shown in Fig. 8a,b. Between 0600–1200 UTC, the layer between the surface and the inversion cooled, as air cooled at the surface was mixed throughout the layer. Above the height Z_{LLJ}, the air warmed since turbulence within the layer was weak, as was shown in Fig. 4b, leading to an intensification of the inversion at 650 m over the night. The shear at the top of the LLJ increased overnight with this increase in static stability.

On 24 October at 0600 UTC, the LLJ was again collocated with an elevated inversion (Fig. 8c), albeit a weaker one where the temperature increased by 0.75 K over 150 m. By 1200 UTC, the stability with the elevated inversion strengthened, as the entire layer below it cooled and the layer above it warmed slightly, as shown in Fig. 8d. Again at 1200 UTC, the height Z_{LLJ} was located at the elevated inversion. The evolution of the LLJ, in relation to the temperature profiles, was different on 9 November (Fig. 8e,f). In both profiles Z_{LLJ} was located at an elevated inversion, but the shape of the LLJ changed over time. Shear in the lowest 200 m increased considerably as static stability also increased over time within the same layer. This is likely due to warm-air advection, which becomes larger with height, and apparently stronger than the vertical redistribution of heat from turbulent mixing. Accurate, precise, and vertically dense measurements of the heat flux and temperature advection would be necessary to determine if advection exceeds the vertical redistribution of heat.

Generally, the height Z_{LLJ} was collocated with an elevated inversion for LLJs associated with a turbulent wSBL. This is due to the fact that the air below Z_{LLJ} remains well-mixed overnight. The wind speed remains sufficiently large during the evening transition and throughout the night, concurrently shear replaces thermal instability as the instability mechanism around sunset. Air cooled near the surface is transported upward, and warmer air from above is mixed downward continuously preventing a surface inversion layer from forming. At and above Z_{LLJ}, mixing is weak and the layer generally warms over time due to the southerly warm-air advection, intensifying the strength of the elevated inversion over time.

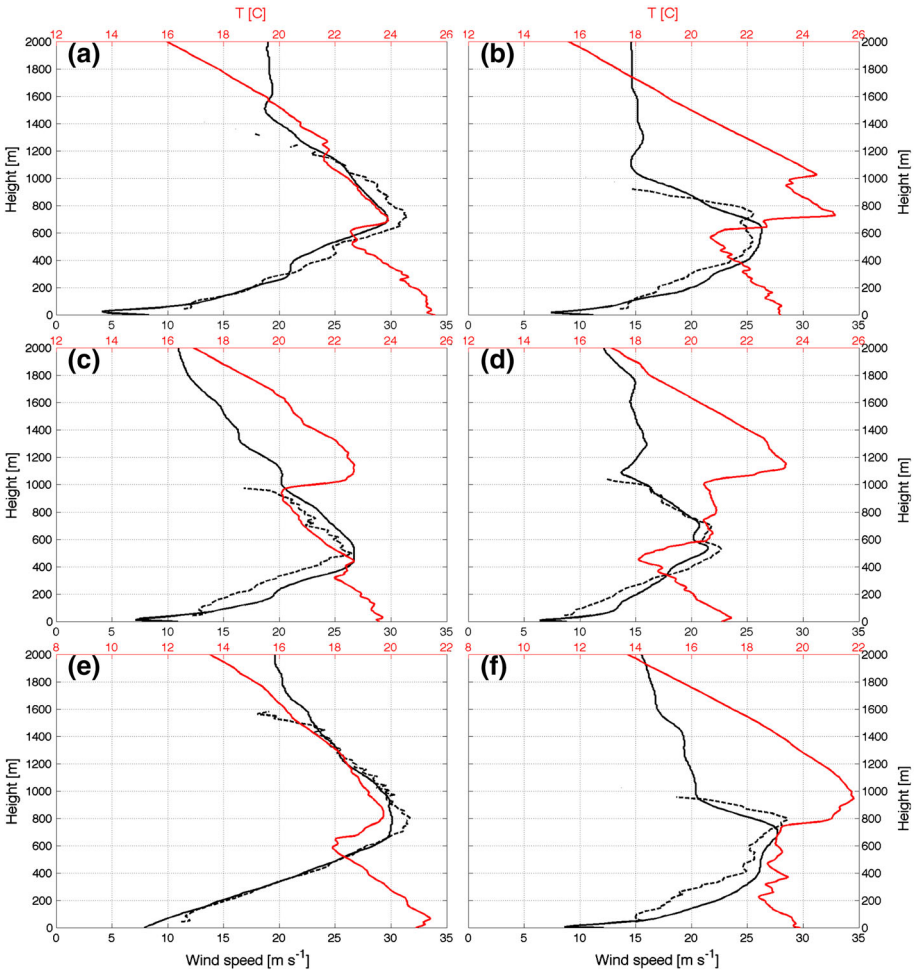

Fig. 8 Profiles of temperature and wind speed during time periods when LLJs were associated with strong near-surface turbulence and a wSBL. Red lines show the temperature measured by the radiosonde, and black shows the wind speed from the OU Doppler lidar (dashed) and radiosonde (solid). Profiles are for the cases discussed in Sect. 3.2: 22 October (**a**, **b**), 24 October (**c**, **d**), and 9 November (**e**, **f**). Left column is from profiles at approximately 0600 UTC, right is at 1200 UTC. Radiosonde and Doppler lidar observations may be up to 15 min apart

5 General Low-Level Jet Differences Based on Boundary-Layer Classification

5.1 Contrasting Evolution of the Low-Level Jet

5.1.1 Evolution of Z_{LLJ} Overnight

The LLJs tended to evolve differently depending on the SBL classification, as shown in Fig. 9 where the mean Z_{LLJ} with its associated standard deviation, as well as Z_{LLJ} values on individual nights, are provided. Early in the night, particularly before 0200 UTC, Z_{LLJ}

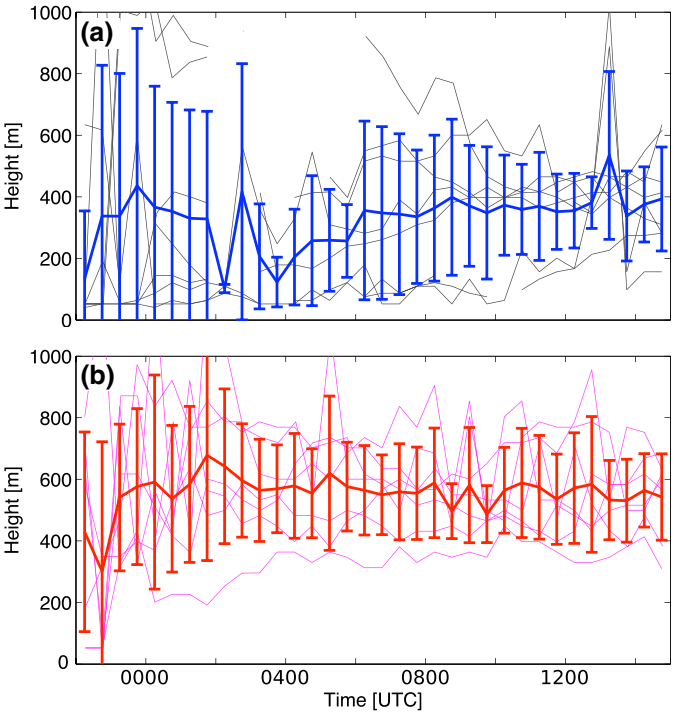

Fig. 9 General time evolution of Z_{LLJ} for eight southerly LLJs associated with a weakly turbulent vSBL (**a**) and seven LLJs associated with a strongly turbulent wSBL (**b**) during the LABLE-I field campaign. Grey and magenta lines denote the time-evolution on individual nights, while the blue and red lines show the mean height and the standard deviation of the jet height. Individual profiles may have large changes in Z_{LLJ} over short time periods when the LLJ is broad and not well-defined, or if multiple LLJs are present at different heights

values are computed even if an LLJ has not yet formed. Specifically, the high values of Z_{LLJ} above 800 m in Fig. 9a are simply maxima in the wind profile prior to LLJ formation.

Generally, LLJs associated with a vSBL showed a greater variation of Z_{LLJ}, particularly early in the night when no substantial wind-speed maximum had yet formed. Additionally, these LLJs tended to originate and form in two different locations. Some of these LLJs formed very close to the surface, often within the lowest 100 m.

However, values of Z_{LLJ} in the vSBL tended to collapse to a similar height by the early morning hours, as shown by the fact that the standard deviation of Z_{LLJ} in Fig. 9a becomes smaller with time. This is likely related to the fact that these LLJs tend to follow isentropic surfaces, as shown in the case studies in Sect. 3.1. As the surface-based nocturnal inversion develops and becomes deeper, the LLJ tends to rise following the isentropic surface. Conversely, the LLJs that originated at higher elevations descend following the isentrope, as the layer of air above 500 m tends to warm from southerly warm-air advection. These effects of differential cooling/warming with height overnight, as discussed in Bonin et al. (2015), tend to cause Z_{LLJ} to trend towards to the height where $d\theta/dt$ is zero.

The height of the LLJs that were associated with a strongly turbulent wSBL evolved differently, as shown in Fig. 9b. The height of the LLJ did not appear to follow isentropic surfaces within the case studies, as the weakly-turbulent LLJs did. This is not surprising, since

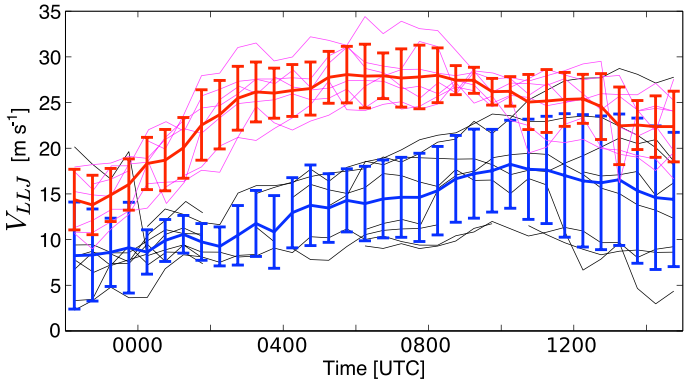

Fig. 10 General time evolution of V_{LLJ} from eight southerly LLjs associated with a vSBL and seven southerly LLJs associated with a wSBL during the LABLE-I field campaign. Blue line and errorbars denote the mean and standard deviation of V_{LLJ} for LLJs associated with a vSBL, where grey lines are time series from individual nights. Red line and errorbars show the mean and standard deviation of V_{LLJ} for LLJs associated with a turbulent wSBL, where magenta lines are time series over individual nights

atmospheric flows only follow isentropic coordinates when diabatic heating and turbulent mixing are negligible (Bluestein 1993). Instead, Z_{LLJ} associated with these LLJs tended to stay roughly constant over the course of the night. This is reflected in both the mean and individual values of Z_{LLJ} in Fig. 9b. Generally, the mean Z_{LLJ} is higher throughout the night for LLJs associated with a turbulent wSBL, as the energy generating eddies are larger and can transport greater momentum.

5.1.2 Evolution of V_{LLJ} Overnight

Just as Z_{LLJ} evolved differently for the two SBL types, the relative strength of the jet also showed distinct progression, as is shown in Fig. 10. For LLJs associated with a vSBL, V_{LLJ} generally increases throughout the night until shortly before sunrise (1000–1200 UTC). This is apparent for both the mean and individual time series of V_{LLJ}. Over the course of the night, variability of V_{LLJ} increases for these LLJs, as shown by standard deviation increasing with time. Early in the night, V_{LLJ} tends to be relatively small ($\approx$10 m s^{-1}) in all of these LLJs. Overnight, V_{LLJ} generally increases by a varying amount, with V_{LLJ} remaining relatively constant throughout the night on some occasions. The reason for discrepancies in how V_{LLJ} evolves is unclear, but is likely related to differences in the synoptic scale forcing. Additionally, these discrepancies may be related to how stability changes over time during the different nights, as discussed in Sect. 5.2.

While V_{LLJ} generally increases for most of the night during LLJs associated with a vSBL, V_{LLJ} typically reaches a maximum value around midnight for LLJs associated with a turbulent wSBL, after which V_{LLJ} slowly decreases throughout the rest of the night. Additionally, all of these LLJs show a similar pattern, as evidenced by the relatively small standard deviation over the entire night. This timing of the maximum V_{LLJ} in a wSBL is consistent with what is expected due to the inertial oscillation (Blackadar 1957).

The boundary-layer wind speed around sunset (2300–0000 UTC) is largest on nights when LLJs form associated with a wSBL. Assuming that V_{LLJ} is representative of the mean wind speed in the well-mixed PBL in this time frame, this indicates the strong wind and large near-surface wind shear generate sufficient turbulence to prevent a surface-based temperature

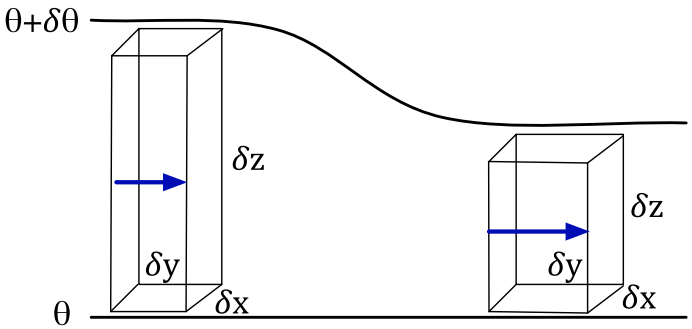

Fig. 11 Schematic of how a volume of air will changes on an isentropic surface

inversion from forming. As no inversion forms to inhibit mixing, turbulence is maintained overnight in a positive feedback cycle. Since the PBL remains turbulent, the dominant terms in the prognostic equations governing the mean flow devolve into a steady state condition, resulting in Z_{LLJ} remaining nearly constant throughout the night.

5.2 Stability Relation

As shown by the case studies in Sect. 3.1 , LLJs associated with a vSBL tend to follow isentropic surfaces. This is unsurprising as isentropic surfaces are material surfaces, across which there is no exchange of mass, when processes are adiabatic (Bluestein 1993). While processes are not adiabatic within the daytime convective boundary layer, there is negligible diabatic heating within the residual layer of the SBL in the absence of clouds and precipitation. This layer is decoupled from the surface with the absence of vertical mixing, so that the sensible and latent heat flux is often small. Thus, it is expected that flows within the residual layer of a vSBL would follow isentropic surfaces just as flows within the free troposphere.

As discussed in Sect. 3.1, the value of V_{LLJ} tends to increase when thermodynamic stability $d\theta/dz$ increases. This strengthening of these weakly turbulent LLJs could be explained by mass conservation following isentropic surfaces. Considering a parcel of air that is located between two isentropic surfaces, as in Fig. 11, that has a mass M of

$$M = \rho \delta x \delta y \delta z, \tag{1}$$

where ρ is the density, δx is its dimension perpendicular to the flow, δy is its dimension along the flow, and δz is its vertical dimension, M will remain constant through time due to the conservation of mass. As the parcel moves with the flow following the isentropic surface, δz will decrease if stability increases over time. As this happens, δx and δy will need to change to conserve mass. If δx does not vary , then δy will need to change to compensate. Using the Rapid Update Cycle analysis for the cases shown in Fig. 12 (not shown), no significant divergence perpendicular to the flow is apparent over northern Oklahoma, indicating that changes in δx are indeed negligible. With δx remaining roughly constant and assuming ρ remains constant as well (any changes would be small, as the LLJ generally remains within the lowest 1 km of the atmosphere), Eq. 1 can be used to relate the volume of air at two times by

$$\delta y_1 \delta z_1 = \delta y_2 \delta z_2, \tag{2}$$

where the subscripts indicate the values at different times. δy_2 can be related to δy_1 though the strain rate by

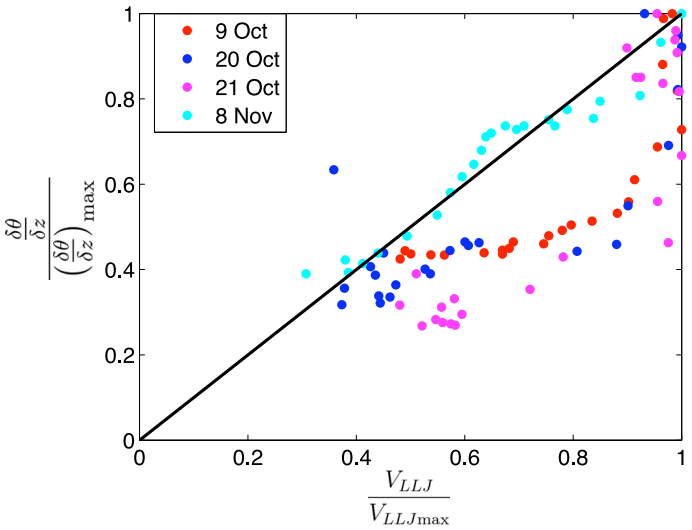

Fig. 12 Relationship of the relative speed of the LLJ (V_{LLJ}) to the maximum wind speed of the LLJ over the night (V_{LLJmax}) with the static stability ($\delta\theta/\delta z$) over the course of the night. Points on the right relate to when the V_{LLJ} was highest in a given night, and points towards the top are when the stability at Z_{LLJ} is the greatest for that night. Data are shown for nights when near-surface turbulence was weak and $Z_{LLJ} > 200$ m. Observations from different nights are coloured differently, with dates given in the legend

$$\delta y_2 = \delta y_1 + \frac{\partial v}{\partial y}\delta y_1 \delta t, \tag{3}$$

where $\partial v/\partial y$ is the change in speed along the flow, and δt is the change in time. By combining Eqs. 2 and 3, the following relationship can be obtained:

$$\delta z_1 = \delta z_2 \left(1 + \frac{\partial v}{\partial y}\delta t\right). \tag{4}$$

By using a time-to-space conversion along with finite differencing, $\partial y = \delta y = v\delta t$ for the time between measurement periods, Eq. 4 can be rewritten as

$$\delta z_1 = \delta z_2 \left(1 + \frac{\delta v}{v}\right), \tag{5}$$

where $\delta v = v_2 - v_1$, using the same subscript notation as earlier. While v is the mean average wind speed between the two measurement periods, v will be assumed to be v_1 for simplicity, which should be valid if the wind speed varies slowly. With this assumption Eq. 5 can be simplified to

$$v_2 = v_1 \frac{\delta z_1}{\delta z_2}, \tag{6}$$

where δz is the depth between two isentropic surfaces at different times. This relationship can be used to show why LLJs associated with a weakly turbulent vSBL strengthen when stability increases. If stability increases over time, $\delta z_1/\delta z_2$ is greater than one, yielding a velocity increase. Additionally, the ratio of v_2 to v_1 is equal to the ratio of δz_1 to δz_2. Thus theoretically, with the assumptions of no divergence perpendicular to the flow, $\delta p/\delta z$ remaining constant, and the pressure gradient remaining constant, V_{LLJ} should vary proportionally to $\delta\theta/\delta z$. In addition to LLJs, the above relationship may also be useful for investigating other atmospheric phenomena and upper-level jets. Although, Eq. 6 should only be used for isentropic flows

for which the pressure level or height changes does not change over time, otherwise changes in ρ will need to be considered as well.

To investigate this relationship with observations, values of $\delta\theta/\delta z$ were compared with values of V_{LLJ} in Fig. 12. Nights when LLJs were associated with a vSBL and where $Z_{LLJ} > 200$ m were used in this analysis. Low-level jets that were located within the lowest 200 m did not appear to follow this relationship as closely, likely due to the fact that diabatic heating for the LLJs was not negligible closer to the surface. Values of $\delta\theta/\delta z$ were calculated from AERI observations, within a layer defined as ± 4 K of θ at Z_{LLJ}. Additionally, values of $\delta\theta/\delta z$ and V_{LLJ} were normalized by their respective maximum values on a given night, for comparison across various nights.

Although the relationship is not entirely clear, V_{LLJ} tends to increase with increasing stability as shown in Fig. 12. Generally, the maximum V_{LLJ} on a given night corresponded to when stability was the highest. Additionally, V_{LLJ} is often much smaller when static stability around it is much weaker. Large scatter in $\delta\theta/\delta z$ is evident for periods when V_{LLJ} is near the maximum. It is unsurprising that the value of V_{LLJ} does not follow the derived relationship of Eq. 6 exactly since the derivation neglects effects of the inertial oscillation, changes in the geostrophic wind, and other mechanisms that alter the flow. Additionally, the increasing stability itself further inhibits mechanical turbulence that mixes momentum vertically, enabling the greater wind shear along the LLJ core in the strengthening LLJ.

6 Conclusions

During the LABLE-I field campaign, many LLJs were observed at the ARM SGP site. The LLJs are grouped into two broad categories based on near-surface values of σ_w, either associated with a weakly turbulent vSBL or strongly turbulent wSBL. Three case studies are shown for each category of LLJ, wherein the evolution of the LLJs is presented and discussed.

Generally, the two categories of LLJs evolved differently overnight and were related to different thermodynamic features. The height of the LLJ generally stayed relatively constant throughout the night for LLJs with a wSBL, and the wind speed reached a maximum around midnight. Low-level jets with a vSBL tended to follow isentropic surfaces by rising overnight if they were initially located near the surface, or descending over time if the LLJ was located over 500 m. These LLJs generally slowly strengthened over the entire night, reaching a maximum in magnitude around sunrise. Additionally, some LLJs associated with a vSBL tended to strengthen overnight as the stability increased. This could be at least partially attributed to the conservation of mass along isentropic surfaces.

While LLJs tended to correspond with inversions in some way, the location of the LLJ consistently varied depending on amount of turbulent mixing. Low-level jets associated with a weakly turbulent vSBL tended to be located at or just above surface-based temperature inversions. One of these LLJs was relatively broad and located distinctly between a surface-based inversion and elevated inversion. Low-level jets associated with a strongly turbulent wSBL tended to be located at the bottom of an elevated inversion. On nights when these LLJs formed, no surface-based inversion was evident in the radiosonde profiles.

Within this study, the wind speed around sunset is observed to be the main factor that differentiate whether an LLJ associated with a wSBL or vSBL forms. This information, along with the analysis of the observed differences in the LLJ characteristics, may be used in refinement of analytical LLJ studies and representation in numerical weather prediction models. Applying a similar analysis to a much larger dataset of several years may allow creation of new LLJ climatologies, which will better identify when certain types of LLJs

are more prevalent. Since this study was confined to the autumn, the LLJs analyzed here are affected by a baroclinic environment and larger synoptic forcing than LLJs in the summer. A different climatology of summertime LLJs would expect to contain a larger percentage of LLJ cases with primarily boundary-layer driven LLJs.

As shown by Smith et al. (2018) and Gebauer et al. (2018), numerical model output can be related to profiler observations to understand the four-dimensional dynamics and structure of the LLJ. Since the analysis here was limited to 2-D cross-sections at one site, expanding this study to include a modeling component will likely elucidate features and mechanisms that are not apparent from this observational analysis alone. This analysis will come in future work.

Acknowledgements We acknowledge everyone that helped to deploy and maintain the instruments during the LABLE-I field campaign. Additionally, we thank Dave Turner and Greg Blumberg for providing and helping interpret the AERI observations. We also thank the four anonymous reviewers for their time and comments, which have led to improvements in the quality of this paper. This study was supported by funding from the Office of the Vice President for Research at the University of Oklahoma. The instruments deployed were in part funded through the NSF Career award ILREUM (NSF ATM 0547882) and the authors received salary support by the National Science Foundation under Grant AGS 1359698. Data from the ARM SGP site were obtained from the Atmospheric Radiation Measurement (ARM) Program sponsored by the U.S. Department of Energy, Office of Science, Office of Biological and Environmental Research, Climate and Environmental Sciences Division.

References

Baas P, Bosveld FC, Baltink HK, Holtslag AAM (2009) A climatology of nocturnal low-level jets at Cabauw. J Appl Meteorol Clim 48:1627–1642. https://doi.org/10.1175/2009JAMC1965.1

Banta RM, Newsom RK, Lundquist JK, Pichugina YL, Coulter RL, Mahrt L (2002) Nocturnal low-level jet characteristics over Kansas during CASES-99. Bound-Lay Meteorol 105:221–252

Banta RM, Pichugina YL, Newsom RK (2003) Relationship between low-level jet properties and turbulence kinetic energy in the nocturnal stable boundary layer. J Atmos Sci 60:2549–2555

Banta RM, Pichugina YL, Brewer WA (2006) Turbulent velocity-variance profiles in the stable boundary layer generated by a nocturnal low-level jet. J Atmos Sci 63:2700–2719

Blackadar AK (1957) Boundary layer wind maxima and their significance for the growth of nocturnal inversions. Bull Am Meteorol Soc 38:282–290

Bluestein HB (1993) Synoptic-dynamic meteorology in midlatitudes, vol I. Oxford University Press, New York

Bonin T, Blumberg W, Klein P, Chilson P (2015) Thermodynamic and turbulence characteristics of the southern great plains nocturnal boundary layer under differing turbulent regimes. Boundary Layer Meteorol 157:401–420. https://doi.org/10.1007/s10546-015-0072-2

Bonner WD (1968) Climatology of the low level jet. Mon Weather Rev 96:833–850

Browning KA, Wexler R (1968) The determination of kinematic properties of a wind field using Doppler radar. J Appl Meteorol 7:105–113

Clarke RH, Smith RK, Reid DG (1981) The morning glory of the gulf of carpentaria: an atmospheric undular bore. Mon Weather Rev 109:1726–1750

Clough SA, Iacono MJ, Moncet JL (1992) Line-by-line calculations of atmospheric fluxes and cooling rates: application to water vapor. J Geophys Res Atmos 97:15,761–15,785

Finnigan JJ, Einaudi F, Fua D (1984) The interaction between an internal gravity wave and turbulence in the stably-stratified nocturnal boundary layer. J Atmos Sci 41:2409–2436

Gebauer JG, Shapiro A, Fedorovich E, Klein P (2018) Convection initiation caused by heterogeneous low-level jets over the Great Plains. Mon Weather Rev 146:2615–2637

Grimsdell AW, Angevine WM (2002) Observations of the afternoon transition of the convective boundary layer. J Appl Meteorol 41:3–11

Holdridge D, Prell J, Ritsche M, Coulter R (2011) Balloon-borne sounding system (SONDE) handbook

Kaplan ML, Lin YL, Charney JJ, Pfeiffer KD, Ensley DB, DeCroix DS, Weglarz RP (2000) A terminal area PBL prediction system at Dallas-Fort Worth and its application in simulating diurnal PBL jets. Bull Am Meteorol Soc 81:2179–2204

Klein P, Bonin TA, Newman JF, Turner DD, Chilson PB, Wainwright CE, Blumberg WG, Mishra S, Carney M, Jacobsen EP, Wharton S, Newsom RK (2015) LABLE: a multi-institutional, student-led, atmospheric boundary-layer experiment. Bull Am Meteorol Soc 96:1743–1764

Klein PM, Hu XM, Xue M (2014) Impacts of mixing processes in nocturnal atmospheric boundary layer on urban ozone concentrations. Boundary-Layer Meteorol 150:107–130

Klein PM, Hu XM, Shapiro A, Xue M (2016) Linkages between boundary-layer structure and the development of nocturnal low-level jets in central Oklahoma. Boundary-Layer Meteorol 158:383–408

Knuteson RO, Revercomb HE, Best FA, Ciganovich NC, Dedecker RG, Dirkx TP, Ellington SC, Feltz WF, Garcia RK, Howell HB, Smith WL, Short JF, Tobin DC (2004a) Atmospheric emitted radiance interferometer. Part 1: instrument design. J Atmos OceanTechnol 21:1763–1776

Knuteson RO, Revercomb HE, Best FA, Ciganovich NC, Dedecker RG, Dirkx TP, Ellington SC, Feltz WF, Garcia RK, Howell HB, Smith WL, Short JF, Tobin DC (2004b) Atmospheric emitted radiance interferometer. Part II: instrument performance. J Atmos OceanTechnol 21:1777–1789

Koch SE, Dorian PB, Ferrare R, Melfi SH, Skillman WC, Whiteman D (1991) Structure of an internal bore and dissipating gravity current as revealed by Raman Lidar

Lenschow DH, Wulfmeyer V, Senff C (2000) Measuring second- through fourth-order moments in noisy data. J Atmos OceanTechnol 17:1330–1347

Mahrt L (1981) The early evening boundary layer transition. Q J R Meteorol Soc 107:329–343

Mahrt L (2014) Stably stratified atmospheric boundary layers. Annu Rev Fluid Mech 46:23–45

Mahrt L, Sun J, Stauffer D (2015) Dependence of turbulent velocities on wind speed and stratification. Boundary-Layer Meteorol 155:55–71

Mitchell MJ, Arritt RW, Labas K (1995) A climatology of the warm season great plains low-level jet using wind profiler observations. Weather Forecast 10:576–591

Newsom RK (2012) Doppler lidar (DL) handbook

Newsom RK, Alan Brewer W, Wilczak JM, Wolfe DE, Oncley SP, Lundquist JK (2017) Validating precision estimates in horizontal wind measurements from a Doppler lidar. Atmos Meas Tech 10:1229–1240

Rodgers CD (2000) Inverse methods for atmospheric sounding: theory and practice. World Scientific

Shapiro A, Fedorovich E (2009) Nocturnal low-level jet over a shallow slope. Acta Geophys 57:950–980

Sisterson DL, Frenzen P (1978) Nocturnal boundary-layer wind maxima and the problem of wind power assessment. Environ Sci Technol 12:218–221

Smith EN, Gibbs JA, Fedorovich E, Klein PM (2018) WRF model study of the Great Plains low-level jet: effects of grid spacing and boundary layer parameterization. J Appl Meteorol Clim 57:2375–2397

Song J, Liao K, Coulter RL, Lesht BM (2005) Climatology of the low-level jet at the southern great plains atmospheric boundary layer experiments site. J Appl Meteorol 44:1593–1606

Stensrud DJ (1996) Importance of low-level jets to climate: a review. J Clim 9(8):1698–1711

Storm B, Dudhia J, Basu S, Swift A, Giammanco I (2009) Evaluation of the weather research and forecasting model on forecasting low-level jets: Implications for wind energy. Wind Energy 12:81–90

Sun J, Mahrt L, Banta RM, Pichugina YL (2012) Turbulence regimes and turbulence intermittency in the stable boundary layer during CASES-99. J Atmos Sci 69:338–351

Turner DD, Löhnert U (2014) Information content and uncertainties in thermodynamic profiles and liquid cloud properties retrieved from the ground-based atmospheric emitted radiance interferometer (AERI). J Appl Meteorol Clim 53:752–771

Turner DD, Knuteson RO, Revercomb HE, Lo C, Dedecker RG (2006) Noise reduction of atmospheric emitted radiance interferometer (AERI) observations using principal component analysis. J Atmos OceanTechnol 23:1223–1238

Van de Wiel BJH, Moene AF, Steeneveld GJ, Baas P, Bosveld FC, Holtslag AAM (2010) A conceptual view on inertial oscillations and nocturnal low-level jets. J Atmos Sci 67:2679–2689

Van de Wiel BJH, Moene AF, Jonker HJJ, Baas P, Basu S, Donda JMM, Sun J, Holtslag AAM (2012) The minimum wind speed for sustainable turbulence in the nocturnal boundary layer. J Atmos Sci 69:3116–3127

Vanderwende BJ, Lundquist JK (2012) The modification of wind turbine performance by statistically distinct atmospheric regimes. Environ Res Lett 7(034):035

Wharton S, Simpson M, Osuna JL, Newman JF, Biraud SC (2015) Role of surface energy exchange for simulating wind turbine inflow: a case study in the Southern Great Plains, USA. Atmosphere 6:21–49

Whiteman CD, Bian X, Zhong S (1997) Low-level jet climatology from enhanced rawinsonde observations at a site in the southern great plains. J Appl Meteorol 36(10):1363–1376